Materials Advances

ROYAL SOCIETY OF CHEMISTRY

PAPER

View Article Online
View Journal | View Issue

Cite this: *Mater. Adv.*, 2026, 7, 2663

gC_3N_4 decorated with ZnO:Mn rods for enhanced photocatalytic performance

Adriana Popa,[a] Maria Stefan,[a] Sergiu Macavei,[a] Lucian Barbu-Tudoran,[ab] Ioana Perhaita,[c] Maria Suciu,[a] Cristian Leostean[a] and Dana Toloman *[a]

In the present research, ZnO:Mn rods obtained from recycled anodic paste of spent Zn–MnO_2 alkaline batteries were immobilized on the surface of graphitic carbon nitride (gC_3N_4) and tested as photocatalysts for degradation of RhB under visible light irradiation. The effect of the ratio between the two components of the composite materials on the RhB removal rate was investigated. The achievement of the composite material was proved by X-ray diffraction (XRD), scanning transmission electron microscopy (STEM), Fourier transform infrared spectroscopy (FTIR), and electron paramagnetic resonance (EPR). The Brunauer–Emmett–Teller (BET) analysis shows that increasing the ZnO:Mn content decreases the surface area of the composite samples. The composite samples show enhanced photocatalytic activity under visible irradiation compared with ZnO:Mn. The sample with the ratio 1–0.1 between gC_3N_4 and ZnO:Mn has the highest removal rate of 93% with a kinetic constant of 12.1 × 10^{-3} min^{-1} almost six times higher than that corresponding to the ZnO:Mn sample (2.3 × 10^{-3} min^{-1}). The superoxide radicals are the main reactive oxygen species (ROS) involved in the dye degradation, as evidence by EPR spectroscopy coupled with the spin trapping technique. The coupling between gC_3N_4 and ZnO:Mn suppresses the electron–hole pair recombination, improving the photocatalytic performance. Moreover, the sample has good stability, and the removal rate was slightly modified after 5 consecutive reaction cycles. Also, the samples have a potential inhibitory antibacterial effect.

Received 27th October 2025,
Accepted 28th January 2026

DOI: 10.1039/d5ma01238d

rsc.li/materials-advances

1. Introduction

Environmental issues concerning water pollution have become a stringent problem worldwide due to globalization and industrialization expansions. A major contribution to environmental pollution is industrial dyestuffs, known as one of the largest groups of organic compound pollutants.[1] In the dyeing process, about 20% of the total dye obtained worldwide is lost and discharged in water bodies without any treatment, thus leading to substantial environmental pollution. These dye pollutants are harmful, dangerous, and potentially mutagenic.[2] Among synthetic dyes, the most used is rhodamine B (RhB), which the World Health Organization cataloged as a category three carcinogen due to its high toxicity, easy accumulation, and stable chemical structure.[3]

Many techniques were developed to treat contaminated water, such as filtration, coagulation, flocculation, adsorption, and physical and chemical methods. Unfortunately, all these methods have limitations in removing organic pollutants and heavy metals.[4] One of the promising technologies for mitigating environmental pollution is photocatalysis, an advanced oxidation process. Photocatalysis has good efficiency in degrading organic contaminants and heavy metal ions. The photocatalytic process is explained by the activation of the semiconductor material by light irradiation with energy equal to or higher than its band gap energy. Thus, electron–hole pairs are generated, which can participate in organic pollutants' oxidation and reduction reactions. Researchers have recently focused on developing photocatalytic materials,[5–7] improving existing catalysts *via* synthesis methods or elaborating new ones.

ZnO, an n-type metal oxide semiconductor, is a common photocatalyst with high oxidation capacity, adjustable size, excellent chemical stability, low toxicity and can be synthesized by different methods. ZnO shows a higher absorption capacity covering a large fraction of the solar spectrum than TiO_2.[8] One of its limitations is a relatively high charge carrier recombination, negatively impacting the photocatalytic reactions. To overcome this limitation, various methods have been applied. Doping with nonmetal and metal ions successfully narrows the band gap, enhances the separation charge carrier, and shifts the wavelength of absorbed light to the visible area.[9,10]

[a] *National Institute for Research and Development of Isotopic and Molecular Technologies, Donat 67-103, Cluj-Napoca, 400293, Romania. E-mail: dana.toloman@itim-cj.ro*
[b] *Electron Microscopy Center, Faculty of Biology and Geology, Babes-Bolyai University, Clinicilor 5-7, 400006, Cluj-Napoca, Romania*
[c] *Babes-Bolyai University, Raluca Ripan Institute for Research in Chemistry, Fantanele 30, Cluj-Napoca, 400294, Romania*

The coupling of ZnO with a narrow energy band gap semiconductor represents another method of enhancing the photocatalytic activity. In this case, a heterostructure is obtained at the interface of the two semiconductors. The photogenerated electrons would move from the semiconductor with a higher conduction band energy to the lower one, enhancing the separation of photogenerated electrons and holes.[11] The coupling between ZnO and g-C_3N_4 was reported as an encouraging solution due to the band structure matching, leading to the accumulation of spatial charges at the interface, facilitating the separation of photogenerated charges. Besides, the obtained composite can be activated by a broad light spectrum, particularly visible light.[12] g-C_3N_4 is a non-metallic semiconductor with high thermal and chemical stability due to the strong covalent bonds between carbon and nitrogen atoms. With a narrow band gap (2.7 eV), g-C_3N_4 can absorb visible light and act as a responsive photocatalyst. Its limits are related to the high recombination process, weak electrical conductivity, and low oxidation ability of holes in the valence band.[13]

Recently, different composite materials based on ZnO and g-C_3N_4 have been reported with enhanced photocatalytic performances under visible light. Hassan *et al.* developed ZnO/g-C_3N_4 S-scheme photocatalysts used for paracetamol degradation, and proved that hydroxyl radicals are the reactive species involved in paracetamol photodegradation.[14] X. Gao *et al.* obtained g-C_3N_4 nanosheets decorated with ZnO nanoparticles by refluxing method at low temperature and obtained composites with enhanced photocatalytic activity.[15] Also, K. Bi *et al.* reported ZnO/g-C_3N_4 S-scheme with effective separation of photogenerated charges and improved photocatalytic material for RhB degradation.[16] These reports indicate that ZnO/g-C_3N_4 composite material has promising potential in wastewater treatment by optimizing the band structure at the composite interface.

In the last years, the waste-derived nanomaterials have represented one of the emerging research areas. Numerous efforts have been made for the nanomaterial's synthesis from diverse biological and industrial wastes. Around 7 billion tons of industrial waste are generated or disposed of annually, which negatively impacts the environment due to their toxic, flammable, corrosive, highly reactive, infectious, and radioactive properties.[17] Consequently, it is important to recycle these industrial wastes to obtain added-value products that benefit environmental safety. About 90% of the total annual transactions of portable batteries worldwide are represented by Zn–Mn batteries. Therefore, recycling Zn from Zn–Mn battery waste fosters the sustainable use of resources and prevents the disposal of these contaminants into the environment. The Zn–Mn battery waste recycling has been used to obtain nanomaterials such as ZnO nanoparticles,[18] nanofibers,[19] *etc.*

Considering the above, this work focuses on preparing gC_3N_4-ZnO:Mn composites with enhanced photocatalytic activity for water depollution under visible irradiation. Mn-doped ZnO particles were obtained from anodic paste of spent Zn–MnO_2 alkaline batteries.[20] The decoration of Mn-doped ZnO particles on the gC_3N_4 surface was realized using poly(allylamine) hydrochloride (PAH) as a linking agent. Various characterization methods characterized the composite samples, and their photocatalytic activity was evaluated using a synthetic RhB solution as a model pollutant. The photocatalytic mechanism was explained based on the EPR spin trapping method results and in correlation with the other characterization techniques. The heterojunction photocatalysts based on Mn-doped ZnO particles and gC_3N_4 exhibit enhanced photocatalytic properties due to the photogenerated charges, which are better separated.

2. Experimental part

2.1. Materials

Melamine-$C_3N_3(NH_2)_3$ (99%, Alfa Aesar) was used as a precursor for obtaining g-C_3N_4. Absolute ethanol-CH_3CHCH_2OH (p.a., Alfa Aesar) and, poly(allylamine hydrochloride)-$[CH_2CH(CH_2NH_2\cdots HCl)]_n$ (PAH, $\geq$99.5%, Alfa Aesar) were employed in the heterojunction process. The ZnO:Mn was generated from a flashlight's discharged Energizer AA alkaline battery. Hydrochloric acid-ZnCl (37% VWR) was used as a leaching reagent. Isopropyl alcohol-CH_3CHCH_2OH (for synthesis, Alfa Aesar) was utilized in the synthesis and scavenger experiments. Also, in scavenger experiments was used vitamin C, L-ascorbic acid-$C_6H_8O_6$ (99%, Sigma-Aldrich). The aqueous solution of Rhodamine B (RhB, $\geq$97%, Sigma-Aldrich) was applied as a pollutant. For demonstrating ROS generation, the following chemical compounds were used: 5,5-dimethyl-1-pyrroline *N*-oxide-$(CH_3)_2C(CH_2)_2$-CHNO ($\geq$97%, DMPO, Sigma-Aldrich), dimethyl sulfoxide-$(CH_3)SO$ ($\geq$99.9%, DMSO, VWR International). The aqueous solutions were prepared with the use of Milli-Q water by the Direct-Q 3UV system (Millipore, Bedford, MA). The solutions were prepared using Milli-Q water using the Direct-Q 3UV system (Millipore, Bedford, MA).

2.2. Preparation of gC_3N_4-ZnO:Mn composites

gC_3N_4-ZnO:Mn composites were made by combining gC_3N_4 and ZnO:Mn in various weight ratios. ZnO:Mn rods were produced by recycling the anode paste from alkaline Zn–MnO_2 batteries, using precise purification techniques and annealing temperatures described in our earlier research.[20] g-C_3N_4 was prepared by thermally decomposing melamine at 550 °C for 3 hours. gC_3N_4-ZnO:Mn composites were obtained utilizing the linking polymer PAH. In the experimental procedure, the g-C_3N_4 (180 mg) was dispersed in a 0.7 wt% PAH salt solution (0.5 M NaCl, 500 mL), sonicated for 4 h, and then stirred overnight at 80 °C. To remove the extra polymer, a centrifugation step was repeated several times. Before decoration, every single component was ultrasonically dispersed for 30 minutes. After mixing both components, the decoration was kept for another 4 hours. The produced gC_3N_4-ZnO:Mn was separated by centrifugation, cleaned with distilled water multiple times, and dried at 65 °C in the oven. For the purpose of this investigation, three samples were synthesized that are distinct from each other in the weight ratio of the component's combination. The samples are named:

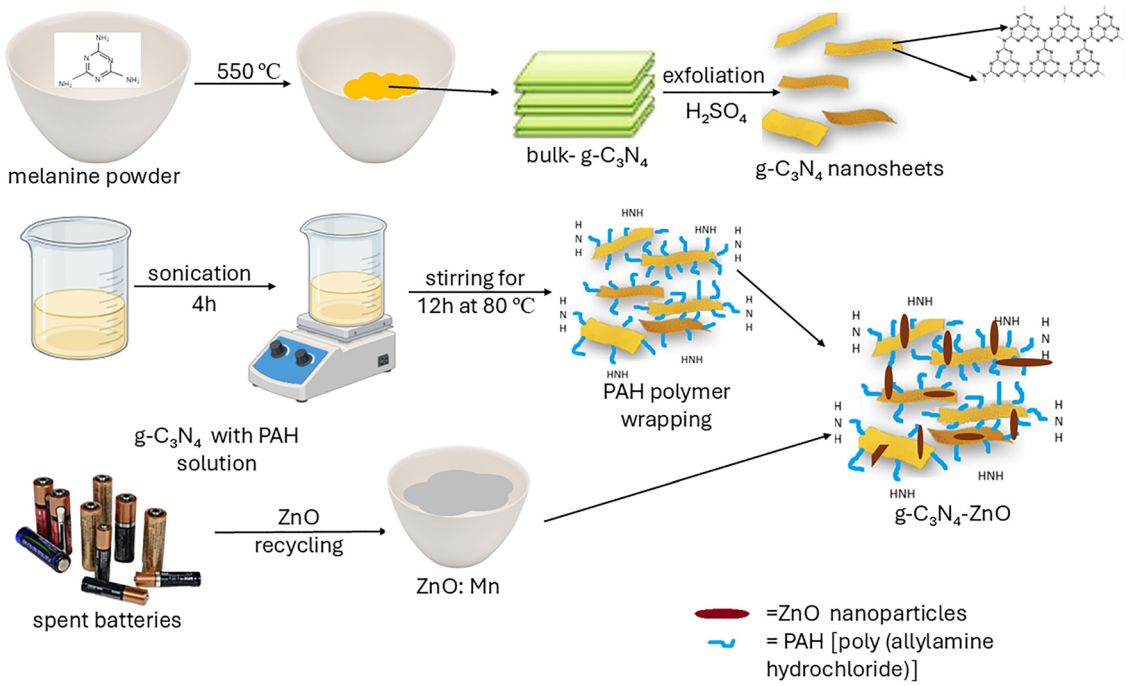

Scheme 1 A simplified diagram illustrating the synthesis procedure.

gC_3N_4-ZnO:Mn_1–0.1; gC_3N_4-ZnO:Mn_1–1; gC_3N_4-ZnO:Mn_1–2. In Scheme 1, the synthesis procedure is shown.

2.3. Characterization techniques

The thermogravimetric TG-DTA-DTG analysis of melamine a precursor for the production of g-C_3N_4 was performed using a Mettler Toledo TGA/SDTA851e equipment in a platinum crucible at a heating rate of 10 °C min^{-1} and a nitrogen flow rate of 60 mL min^{-1}. XRD measurements were done by a Rigaku SmartLab automated multipurpose Diffractometer with Cu-Kα radiation (λ = 1.5406 Å), operating at 45 kV and 200 mA. The diffractometer is equipped with a D/tex Ultra 250 detector monochromator. The diffractograms were registered in the 2θ range of 10°–80° and with steps of $\Delta\theta$ = 0.02°. For diffractogram processing, the PDXL2: Integrated X-ray powder software was used. The sample morphology was investigated using a STEM Hitachi HD2700 Electron Microscope equipped with a cold field emission gun, operating at 200 kV. Specific surface area and porosity measurements were collected with a Micromeritics, TriStar II 3020-surface area and porosity analyzer to determine material textural characteristics. The adsorption–desorption isotherms were measured around the boiling point of nitrogen (77 K). The FT-IR spectra were measured in the spectral range of 400–4000 cm^{-1} and with a spectral resolution of 2 cm^{-1} using a JASCO 6100 FT-IR spectrometer. Optical properties were investigated using UV-vis absorption spectra recorded with a JASCO V570 UV-vis-NIR Spectrophotometer equipped with an absolute reflectivity measurement JASCO ARN-475 accessory in a wavelength range of 190–900 nm. The absorbance spectra were obtained from the reflectance spectra using the internal software. The photoluminescence (PL) analysis was conducted on an FS5 Spectrofluorometer from Edinburgh Instruments equipped with a 150 W CW Ozone-free Xenon arc lamp, Czerny–Turner with plane grating monochromators, and a PMT-900 emission detector. The spectra are measured at room temperature with a 325 nm (3.81 eV) excitation wavelength. EPR spectroscopy measurements were carried out on a Bruker E-500 ELEXSYS X-band (9.87 GHz) spectrometer at room temperature under identical conditions using equal quantities of samples. X-Ray Photoelectron Spectroscopy (XPS) valence band analysis was performed with a custom-build SPECS spectrometer working with Al anode (1486.6 eV).

2.4. Photocatalytic activity evaluation

The photocatalytic activity was tested under visible light irradiation using a synthetic RhB solution. The tests were done in a custom-built laboratory-visible reactor system having a 400 W halogen lamp (Osram) and a magnetic stirrer. 10 mg of catalyst were mixed in 10 mL aqueous solution of RhB (1.0×10^{-5} mol L^{-1}) and stirred in the dark for 2 h to reach the adsorption equilibrium on the catalyst surface. Each degradation experiment was performed for 3 h. About 3.5 mL was extracted every 60 min, the catalyst was separated from the suspensions with a permanent magnet, and analyses were made using a UV-vis spectrometer by recording the pollutant-specific maximum absorbance. Photocatalytic activity is calculated using eqn (1):

$$\text{Photocatalytic activity}\ (\%) = \frac{A_0 - A_t}{A_0} \times 100 \qquad (1)$$

where, A_0 and A_t represent the initial and the absorbance at time t, respectively.

ROS generation was evidenced by EPR spectroscopy coupled with the spin trapping method. As spin trapping reagent was used DMPO. 10 mg of composite sample was dispersed in DMSO (1 mL) and homogenized in an ultrasound bath (30 min) before use. DMPO of 0.2 mol L^{-1} concentration was added to the above mixture. The fresh prepared samples were immediately transferred into the quartz flat cell optimized for liquids measurements. All tests were performed in the same conditions.

To evidence the active species involved in the photocatalytic degradation process of RhB under visible irradiation, the scavenger experiments were performed. The following scavengers were used vitamin C for superoxide radical, and isopropyl alcohol for hydroxyl radical. In this experiment was added scavenger agents to the initial solution keeping the photodegradation experiments described above identical.

The stability of the sample was analyzed using reutilization tests. Before each run, the catalyst was recovered by centrifugation and then thoroughly washed with water and ethylic alcohol and dried overnight.

Bacterial cytotoxicity. *Escherichia coli* (ATCC 25922) and *Staphylococcus aureus* (ATCC 12598) colonies were collected from Muller-Hinton-Agar media and resuspended in 0.9% saline solution to a density of 0.5 McF. From this inoculum, new MH-Agar plates were seeded using sterile cotton swabs and then sterile cotton disks were applied on top for the disk diffusion method. The 10 mg mL^{-1} gC_3N_4-ZnO:Mn_1–0.1 disks were placed on the agar medium and the cotton disks were impregnated with 100 μL of 10 mg mL^{-1} RhB and with 10 mg mL^{-1} gC_3N_4-ZnO:Mn_1–0.1 resulting solution. Antibiotics pre-loaded disks were used as controls: kanamycin 30 μg mL^{-1}, gentamycin 10 μg mL^{-1}, ciprofloxacin 5 μg mL^{-1}. Plates were placed in the incubator in dark conditions at 37 °C for 24 hours, after which the developed hallows were measured and the plates were photographed.

3. Results and discussions

3.1. Morpho-structural and textural characteristics

Thermal analysis of melamine was carried out to estimate the decomposition temperature of the precursor used to produce gC_3N_4. Fig. 1 shows TG-DTA-DTG curves of melamine. Melamine exhibits a considerable mass loss at 362 °C, which is accompanied by an exothermic response, possibly caused by the release of a significant amount of ammonia.[21] After this temperature, the sample stabilizes without undergoing any substantial thermal reactions.

To investigate the structure of the composite materials, XRD characterization was performed. The obtained XRD patterns corresponding to gC_3N_4-ZnO:Mn composites samples are shown in Fig. 2a in comparison with the specific patterns of gC_3N_4 and ZnO:Mn. The XRD patterns of all prepared composite materials reveal the presence of ZnO specific peaks indexed with the wurtzite hexagonal structure (PDF 01-070-8072). In addition to these, the diffractograms contain a pronounced peak at 27.4° characteristic of graphitic systems (PDF 00-050-1249).

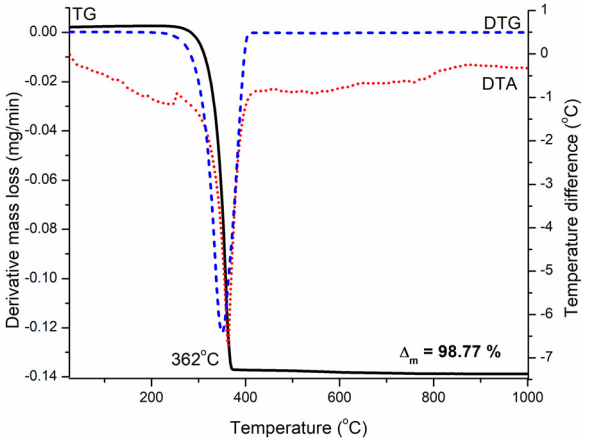

Fig. 1 TG-DTA-DTG curves for melamine as precursor for synthesis of gC_3N_4.

The peak located at 27° was assigned to the interplanar stacking peak of the aromatic systems indexed to the (002) peak.[22,23] No characteristic peaks of secondary phases of other impurities were observed. For ZnO, the mean crystallite size is about 140 nm; the evaluation was made by the Williamson–Hall (W–H) method.

FT-IR spectroscopy was performed to obtain more structural information about the functional groups on the sample's surface. In Fig. 2b are illustrated the spectra corresponding to gC_3N_4-ZnO:Mn_1–2 compared with the spectrum of gC_3N_4. The gC_3N_4 spectrum analysis indicates the presence of an intense band located at 1637 cm^{-1},[24] due to C=N stretching and several bands in the range of 1544 cm^{-1} and 1235 cm^{-1} attributed to the vibration modes of the C–N bonds from the CN aromatic unit.[24] It can also be observed the existence of a band located at 807 cm^{-1} specific to the triazine units from gC_3N_4.[25] The composite clearly displays all of the FTIR vibration peaks associated with gC_3N_4, which shows that the structure of gC_3N_4 remains unmodified during the decoration process. Moreover, the composite samples contain a supplementary band located in the range 400–600 cm^{-1}, which is specific to the vibration of the Zn–O bond.[26]

The EPR spectroscopy was used to prove the paramagnetic species in the composite samples; the obtained spectra for all the samples are displayed in Fig. 3a. To get deep insight into the paramagnetic species responsible for the obtained resonance signals, a simulation of the spectrum corresponding to gC_3N_4-ZnO:Mn_1–2 sample was performed (Fig. 3b). From the simulation analysis results that resonance signals are due to the overlapping of three resonance signals. Signal S1, consisting of a well-resolved hyperfine structure characteristic of isolated Mn^{2+} ions, originated from the interaction between the $S = 5/2$ electronic spin and the $I = 5/2$ nuclear spin of the ^{55}Mn nucleus. The following Hamiltonian parameters: g-tensor, g = 2.0018, hyperfine coupling constant, A = 222 MHz, and zero-field parameter, D = 702 MHz were used for simulation. Signal S2, a sharp one, with a linewidth of 6 G situated at $g \sim 2.006$, is attributed to the generation of unpaired electrons in the localized π-conjugated structure of gC_3N_4.[27,28] The broad resonance line signal S3 is probably due

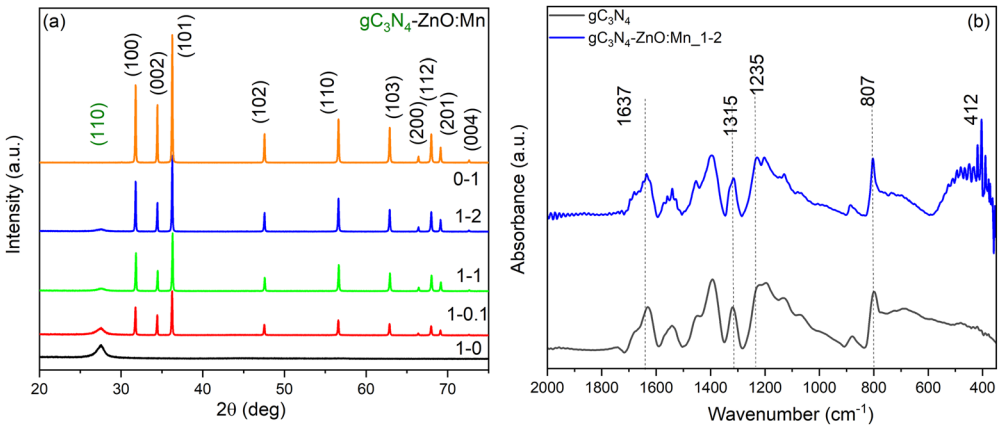

Fig. 2 Diffraction patterns of gC_3N_4-ZnO:Mn composites sample (a); FT-IR spectra of gC_3N_4 and gC_3N_4-ZnO:Mn_1–2 composite sample (b).

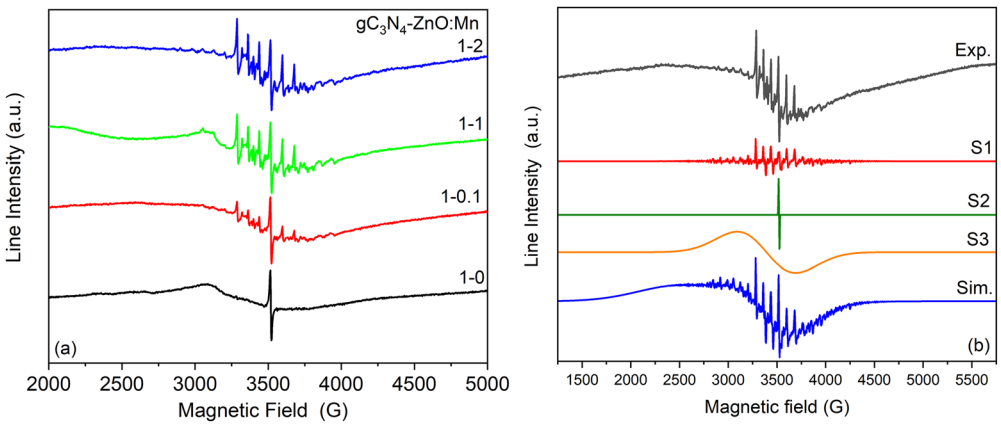

Fig. 3 Experimental EPR spectra of gC_3N_4-ZnO:Mn samples (a); experimental and simulated EPR spectra of gC_3N_4-ZnO:Mn_1–2 sample (b).

to some agglomerated Mn^{2+} ions.[29] The presence of Mn^{2+} ions is due to the inter-contamination between the anode and cathode from the spent batteries.[20]

Morphological characteristics were investigated by SEM and TEM microscopy. Fig. 4a and b are illustrated, as examples of SEM and TEM images for the gC_3N_4-ZnO:Mn_1–1 sample. The SEM and TEM images indicate the presence of both gC_3N_4 layers and ZnO particles. The ZnO particles have a rod shape with the length varying between 500 nm and 1.5 μm and a thickness of 200 nm. Similar morphology and particle size were observed for all samples. To confirm the presence of both components, the elemental mapping was performed by EDS (Fig. 4c). The following elements were evidenced: N and C atoms from gC_3N_4 layers and Zn, O atoms from ZnO particles.

The specific surface area and porosity measurements were carried out because porosity can significantly impact the specific properties of materials. The porosity of the samples was measured according to Barrett, Joyner, and Halenda (BJH) method and adsorption/desorption procedures. The porosity analysis reveals varied characteristics of composite samples concerning the synthesis conditions, as illustrated in Fig. 5(a–d).

The investigated samples exhibit similar isotherms of type III, which are typical of low-porous adsorbents, and the hysteresis created by the two adsorption–desorption isotherms is of type H3. This type of hysteresis appears in aggregates of flat particles or adsorbents with crack-like pores. The pore volume distribution curves as a function of diameter exhibit a multimodal shape, indicating the presence of dimensionally irregular pores. As the gC_3N4-ZnO:Mn ratio increases, the pore volume increases from 0.115 $cm^3\ g^{-1}$ (gC_3N_4) to 0.261 $cm^3\ g^{-1}$ (gC_3N_4-ZnO:Mn_1–1), then drops dramatically to 0.054 $cm^3\ g^{-1}$ at a ratio of 1 : 2. The gC_3N_4 sample's maximum at 31 nm indicates a high level of mesopores ($D < 50$ nm). At a ratio gC_3N4-ZnO : Mn of 1 : 0.1, the mesopores (32 nm) clog slightly and become shorter, but unlike the gC_3N_4 sample, macropores (275 nm) predominate, as seen by an increase in the average pore diameter from 31.15 nm (gC_3N_4) to 92.04 nm (1 : 0.1). At a 1 : 1 ratio of components, the pores get longer, with macropores (97 nm) dominating. When the ratio gC_3N_4-ZnO : Mn is 1 : 2, the pores clog, and the messo-macropore ratio equalizes. The specific surface area of the composite samples decreases by increasing the content of ZnO:Mn from 13.64 $m^2\ g^{-1}$ in case of gC_3N_4 to 4.78 $m^2\ g^{-1}$ for gC_3N_4-ZnO:Mn_1–2 due to the

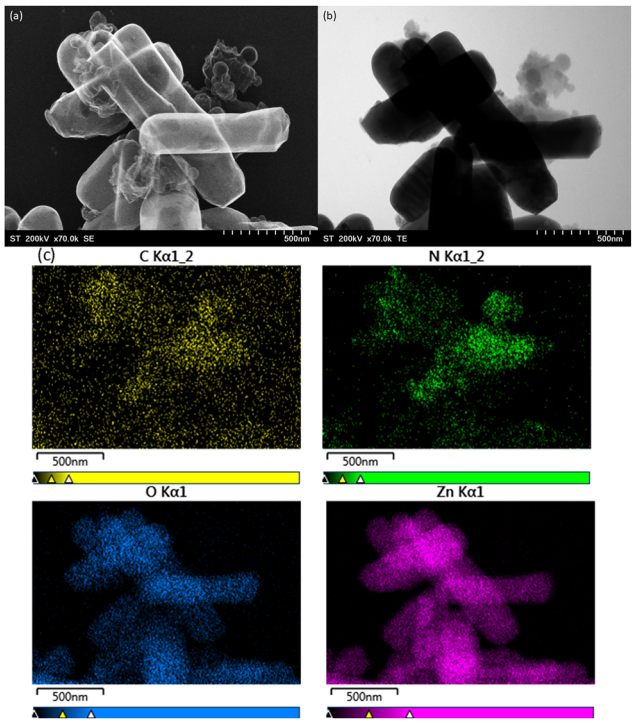

Fig. 4 SEM (a), TEM (b), and the corresponding mapping (c) images for gC_3N_4-ZnO:Mn_1–1.

gC_3N_4 pore blocking by the addition of ZnO:Mn. Table 1 illustrates the main characteristics, including the surface areas (S_{BET}), pores volume, and pores diameter of all the samples.

3.2. Optical properties

The optical properties of the composite materials were evaluated by UV-vis spectroscopy. The absorption spectra of the samples are displayed in Fig. 6a. The ZnO:Mn sample shows an intense and narrow response with a maximum absorption edge at 396 nm, while the optical response of gC_3N_4 presents a broader absorption band with a maximum absorption edge at 470 nm. The gC_3N_4-ZnO:Mn composite samples exhibit two characteristic absorption peaks, one associated with ZnO:Mn and the other with gC_3N_4, confirming the formation of composite samples. As was expected, by increasing the quantity of gC_3N_4, the optical response of composite samples is red-shifted, visible light response being improved, which is beneficial for the visible light photocatalytic process. The band gap's energy of the samples was calculated from Tauc's curves (Fig. 6b). gC_3N_4 has a band gap energy of 2.75 eV similar with the previously reported value,[30] and the value for ZnO:Mn is 3.16 eV. In the case of composite samples, the band gap energy increases by increasing the amount of ZnO:Mn from 2.78 eV for gC_3N_4-ZnO:Mn_1–0.1 sample to 3.12 eV for gC_3N_4-ZnO:Mn_1–2. This tendency was expected since the energy band gap of ZnO:Mn is higher than that of gC_3N_4.

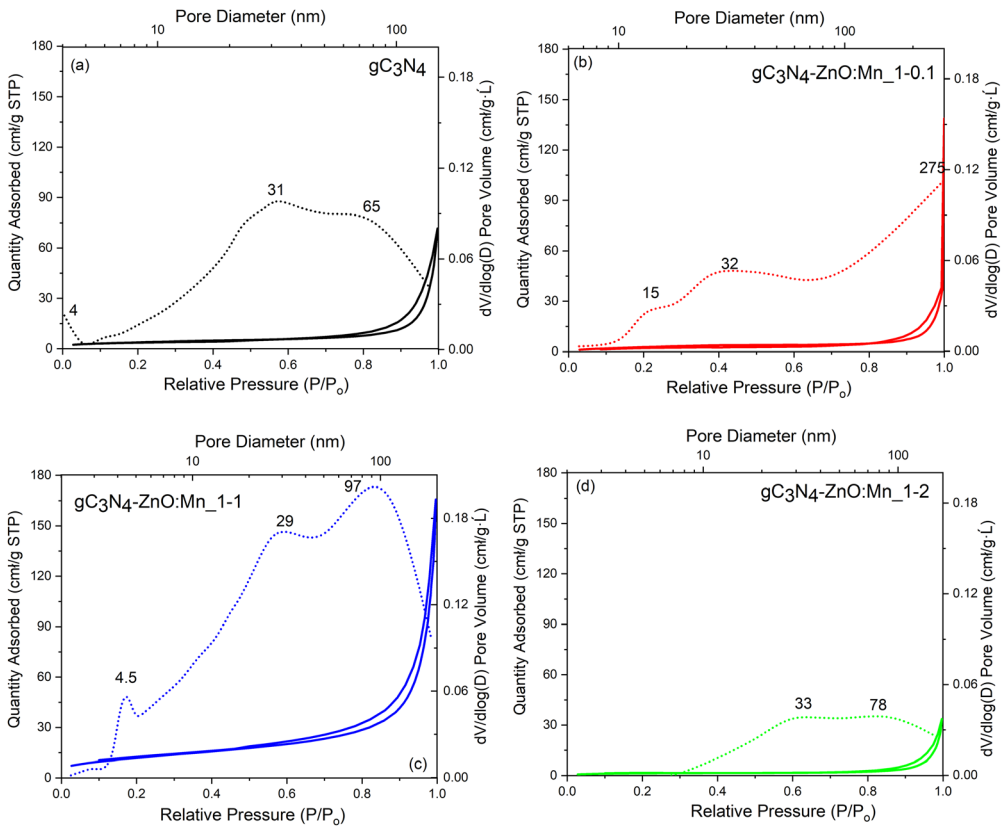

Fig. 5 N_2 adsorption/desorption isotherm and pore size distribution (BJH) of gC_3N_4 (a), gC_3N_4-ZnO:Mn_1–0.1 (b), gC_3N_4-ZnO:Mn_1–1 (c), and gC_3N_4-ZnO:Mn_1–2 samples (d).

Table 1 The samples' surface area (S_{BET}), pores volume, and pores diameter

Sample	S_{BET} ($m^2\ g^{-1}$)	Pores volume ($cm^3\ g^{-1}$)	Pores diameter (nm)
g-C_3N_4	13.64	0.115	31.15
gC_3N_4-ZnO:Mn_1–0.1	11.38	0.218	92.04
gC_3N_4-ZnO:Mn_1–1	12.57	0.261	24.76
gC_3N_4-ZnO:Mn_1–2	4.78	0.054	41.44
ZnO:Mn	2.60	0.018	33.6

Photoluminescence analysis was used to assess the samples' e-h separation efficacy. Photoluminescence emissions on semiconductors result from the radiative recombination of photoelectrons and produced holes.[31] Fig. 6c shows the PL spectra of the gC_3N_4-ZnO:Mn composite samples compared with that of gC_3N_4 obtained using an excitation wavelength of 325 nm. The PL spectra are similar for all the samples and consist of a broad emission band covering the blue-violet to green light region. The experimental spectra were deconvoluted using a Gaussian fitting function to highlight the emission bands and their assignment better. Fig. 6d shows, as an example, the spectrum of gC_3N_4 obtained after deconvolution. The deconvolution of the gC_3N_4 sample reveals the presence of three bands located at 454 nm, 489 nm, and 543 nm. According to previous PL studies, the luminescence properties of gC_3N_4 are due to the energy states of sp^3 hybridized C–N σ band, sp^2 C–N π band, and the lone pair (LP) of the bridging nitrogen atom. Thus, the PL emission band centered at 454 nm was attributed to the σ*–LP transition, while the emission band at 489 nm was related to the transition of the electrons relaxed at π* and LP state, and that at 543 nm to π*–π band transition.[32,33] By decorating gC_3N_4 with ZnO:Mn, the emission is quenched, meaning that the recombination process is delayed, so the photogenerated charges are better separated, beneficial for the photocatalytic process.

3.3. Photocatalytic activity

The photocatalytic properties were evaluated against a RhB synthetic solution under visible irradiation. The photocatalytic activity was monitored by analyzing the UV-vis maximum absorption of RhB. Every 60 min, a 3 mL solution was extracted and separated from the suspension, and the specific absorbance was registered. Fig. 7a shows the removal rate of the samples. All the samples show both adsorption and photocatalytic activity. The adsorption capacity of ZnO:Mn is 16%, and combining ZnO:Mn with gC_3N_4 increases to about 24%. This result was expected since the specific surface of composite samples evaluated from BET experiments decreases by increasing ZnO:Mn content in composite samples.

The composite samples show enhanced photocatalytic activity under visible irradiation compared with ZnO:Mn. The sample with the lower content of gC_3N_4 has the highest removal rate

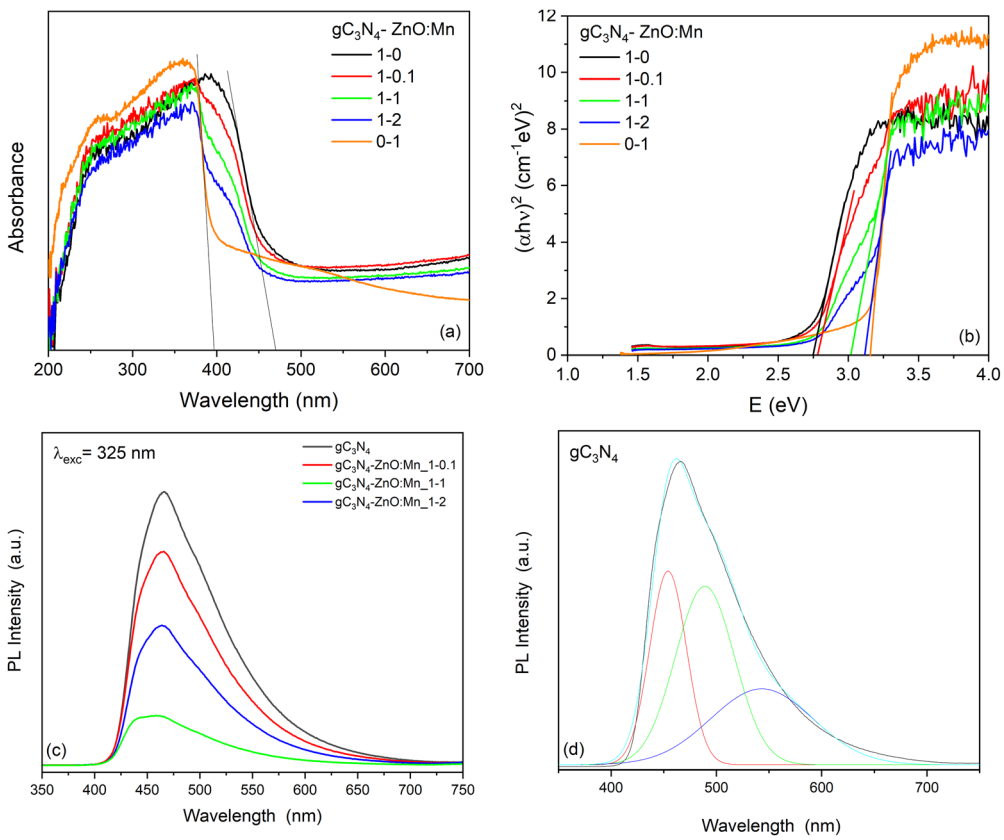

Fig. 6 UV-vis spectra (a); Tauc's plots (b); PL spectra (c) of gC_3N_4 and gC_3N_4-ZnO:Mn samples; and PL spectra of the gC_3N_4 sample together with deconvoluted peaks (d).

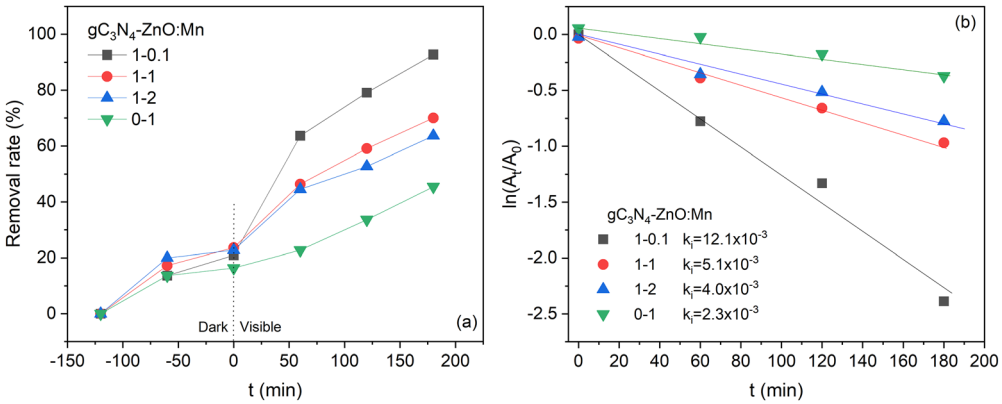

Fig. 7 Removal rate of the samples (a); evaluation of the photodegradation kinetics (b).

of 93%. To describe the photocatalytic process first-order kinetic model was applied, and the obtained plots are illustrated in Fig. 7b; the obtained kinetic constants are inserted in the inset. Indeed, gC_3N_4-ZnO:Mn_1–0.1 has the best removal rate, with the kinetic constant being almost six times higher than that corresponding to the ZnO:Mn sample.

To evaluate the photocatalytic mechanism, the reactive oxygen species generated by the samples were evidenced by EPR spectroscopy coupled with the spin trapping method. The sample with the best photocatalytic activity was chosen to evidence the ROS generation, and as a spin trapping agent, DMPO was used. Before irradiation, no spectrum was obtained, but after 25 min of visible light irradiation, as observed in Fig. 8a, a spectrum composed of several components was obtained. To extract the components' spectrum, a simulation was performed.

The linear combination of the following spin adducts was obtained: $^{\bullet}$DMPO-O_2^- (a_N = 12.8 G, a_H^{β} = 10.4 G, a_H^{γ} = 1.39 G,

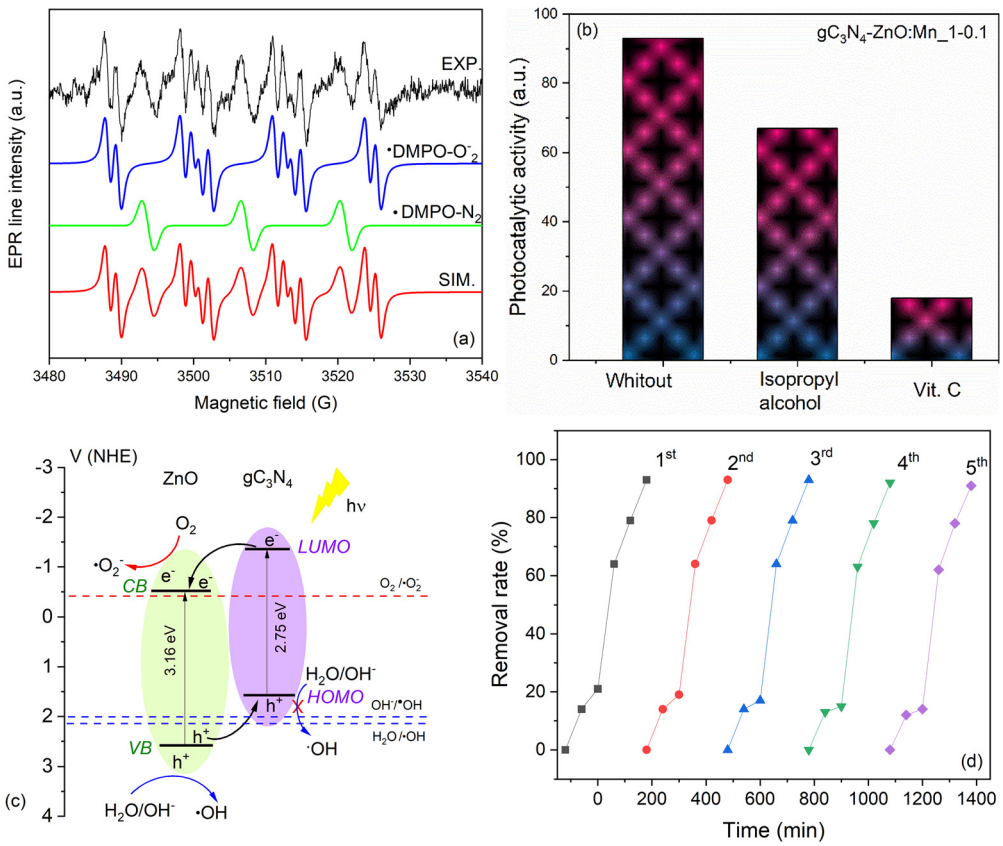

Fig. 8 EPR spectrum of DMPO adducts obtained by irradiating the gC_3N_4-ZnO:Mn_1–0.1 sample (a); removal rate of the gC_3N_4-ZnO:Mn_1–0.1 sample in the presence of different scavengers (b); the proposed photocatalytic mechanism (c); the reusability tests of gC_3N_4-ZnO:Mn_1–0.1 sample (d).

Table 2 Comparison of the photocatalytic activity of various g-C_3N_4/ZnO based photocatalyst

Catalyst	Light source	Pollutant	Irradiation time (min)	Degradation (%)	Kinetic ct. (min^{-1})	Ref.
g-C_3N_4/ZnO	Visible	MB	60	76	0.023	36
g-C_3N_4/ZnO:Ni	Solar	MB	70	100	0.031	37
g-C_3N_4/ZnO	Solar	Paracetamol	60	95	0.052	38
g-C_3N_4/ZnO	Visible	MB	240	—	0.007	39
g-C_3N_4/ZnO:Mn	Solar	MB	60	98	0.032	40
g-C_3N_4/ZnO:Mn	Visible	RhB	180	93	0.012	Present work

g ~2.009) and $^{\bullet}$DMPO-N_2 (a_N 14 G, g ~2.009). Superoxide radicals $^{\bullet}O_2^-$ results from the interaction between the photogenerated electrons and adsorbed O_2. The second component is $^{\bullet}$DMPO-N, which appears by the N–C bond cleavage of DMPO.[34] This result indicates that the sample generates superoxide radicals $^{\bullet}O_2^-$ under visible irradiation, which means that the CB position is more negative than the potential of $O_2/^{\bullet}O_2^-$, it doesn't generate hydroxyl radicals, probably because the VB position is less positive than the potentials of $H_2O/^{\bullet}OH$ and $OH^-/^{\bullet}OH$.[28]

The scavenger experiments were conducted to identify the reactive oxygen species involved in the photodegradation of RhB. Vitamin C was used as a scavenger for $^{\bullet}O_2^-$, while isopropanol targeted $^{\bullet}OH$. To check influence of the scavenger concentration on the photocatalytic activity of the gC_3N_4-ZnO:Mn_1–0.1 sample, the concentration of the scavenger agents was varied between 3 to 7 mM for vitamin C and 60 to 140 μL/10 mL RhB solution for isopropanol. The obtained results are shown in Fig. S1. As was expected an increased concentration of the scavenger agent results in higher inhibition of the photocatalytic activity. As an example, Fig. 8b shows the photocatalytic activity of gC_3N_4-ZnO:Mn_1–01 sample in the absence and presence of 5 mM vitamin C and 100 μL isopropanol added to the initial RhB solution. The addition of both scavengers induced a decrease in the photodegradation rate. Notably, vitamin C caused the most significant inhibition of RhB degradation, indicating that while both reactive species contribute to the process, $^{\bullet}O_2^-$ plays the dominant role.

Consequently, the proposed photocatalytic mechanism is the following: when visible light irradiates the composite sample, the electrons from the valence band (VB) of gC_3N_4 are excited to its conduction band (CB). Because the g-C_3N_4 LUMO edge potential is more negative compared with that of ZnO, the photoinduced electrons from the LUMO of g-C_3N_4 will be transferred easily to that of ZnO *via* the interface,[35] and here they will react with the O_2 molecules adsorbed on the photocatalyst surface, generating superoxide radicals able to degrade the pollutant molecules. At the same time, the holes from the VB of ZnO migrate to the HOMO of g-C_3N_4, but since its position is lower than the oxidation potential of $H_2O/^{\bullet}OH$ and $OH^-/^{\bullet}OH$ redox pair, these reactions may not take place. Thus, only the remaining holes in the ZnO VB could participate in oxidation reactions. The proposed scheme of the photocatalytic mechanism obtained based on the valence band position evaluated by XPS (Fig. S2) and energy band gap values, and ROS generated by the sample is illustrated in Fig. 8c.

Furthermore, the reusability of the sample possessing the best photocatalytic activity (gC_3N_4-ZnO:Mn_1–0.1) was evaluated and illustrated in Fig. 8d. Only a slight decline in photocatalytic activity is observed after five consecutive reaction cycles measured under the same conditions, indicating that the prepared composites maintain good stability. The chemical stability of the photocatalyst was analyzed using XRD and FT-IR. Fig. S3 and S4 illustrate the XRD diffractogram and FT-IR spectra of the gC_3N_4-ZnO:Mn_1–0.1 sample before and after reusability tests showing no modification of the sample crystalline structure, sustaining its excellent chemical stability.

To highlight the potential application of the sample as visible light photocatalyst, the photocatalytic performance of the gC_3N_4-ZnO:Mn_1–0.1 sample was compared with reported studies. Table 2 shows the comparison of the photocatalytic activity of various g-C_3N_4/ZnO based photocatalyst. The results show that gC_3N_4-ZnO:Mn_1–0.1 sample photocatalytic performance is comparable to those obtained in the literature with the specification that the current state of the tests was done on RhB, and the results in the literature were obtained using other types of pollutants.

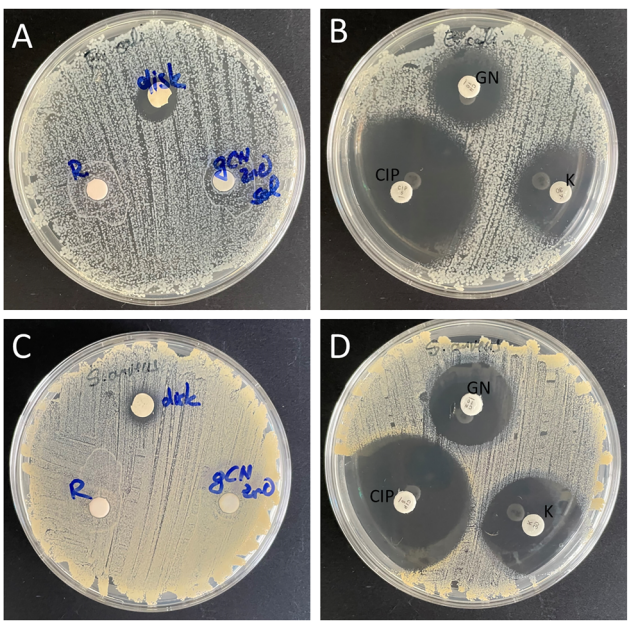

Fig. 9 Cytotoxicity studies on *Escherichia coli* (A) and (B) and *Staphylococcus aureus* (C) and (D) by disk diffusion test. disk = gC_3N_4-ZnO:Mn_1–0.1, 10 mg pressed disk, R = RhB, gC_3N_4-ZnO:Mn_1–0.1 sol = 10 mg mL^{-1} gC_3N_4-ZnO:Mn_1–0.1 solution, K – kanamycin, GN – gentamycin, CYP – ciprofloxacin.

3.4. Bacterial cytotoxicity

To evaluate the bacterial cytotoxicity of the samples and RhB solution were used *Escherichia coli*, a Gram-negative bacterium and *Staphylococcus aureus*, a Gram-positive bacterium. The results of disk diffusion test are shown in Fig. 9. It can be observed that the gC_3N_4-ZnO:Mn_1–0.1, 10 mg pressed disk developed a small inhibition hallow for both bacterial species (A&D) indicating a small antibacterial effect by disk diffusion, slightly larger for the case of *E. coli* (diameter of 15.3 ± 0.7 mm) in comparison to *S. aureus* (12.6 ± 0.6 mm). The 10 mg mL^{-1} RhB solution had no effect on bacteria and the 10 mg mL^{-1} gC_3N_4-ZnO:Mn_1–0.1 solution produced a small and incomplete inhibition hallow for the case of *E. coli* (18.8 ± 1.5 mm), but not for *S. aureus* (A&D). The antibiotics controls presented large inhibition hallows, as expected (Fig. 9B and E): ciprofloxacin (*E. coli*: 54.4 ± 2.6 mm; *S. aureus*: 48 ± 2.9 mm), kanamycin (*E. coli*: 33.6 ± 1.2 mm; *S. aureus*: 35.3 ± 0.4 mm), gentamycin (*E. coli*: 26.6 ± 1.1 mm; *S. aureus*: 29.2 ± 0.4 mm).

4. Conclusions

In this study, a heterojunction based on ZnO:Mn rods obtained by recycling the spent Zn–MnO_2 alkaline batteries and gC_3N_4 were successfully prepared. The TEM image indicates the presence of both gC_3N_4 layers and ZnO particles with a rod shape. XRD and FT-IR support the heterojunction formation. Besides, EPR results evidence unpaired electrons in the localized π-conjugated structure of gC_3N_4 and Mn^{2+} ions present as impurities in ZnO particles. The specific surface area of the composite samples, evaluated by BET analysis, decreases with increasing the content of ZnO:Mn. The photoluminescence characterization shows that decorating gC_3N_4 with ZnO:Mn, the emissions are quenched, meaning that the recombination process is delayed, so the photogenerated charges are better separated, beneficial for the photocatalytic process. The 1–0.1 ratio between gC_3N_4 and ZnO:Mn assures the best removal rate (94%) of RhB under visible light irradiation, higher than that of ZnO:Mn (45%). The significant improvement of the photocatalytic activity was due to the formation of a heterojunction between ZnO:Mn and gC_3N_4, which broadens the spectral response and reduces the recombination of the photogenerated charges. The superoxide radical $^{\bullet}O_2^-$ resulted of the interaction between the photogenerated electrons and O_2 molecules from water is the main reactive oxygen species generated by the gC_3N_4-ZnO:Mn sample. Moreover, the sample has good stability, and the removal rate was slightly modified after 5 consecutive reaction cycles. gC_3N_4-ZnO:Mn_1–0.1 sample has a potential inhibitory antibacterial effect against *E. coli* and less so against *S. aureus*. RhB by itself did not induce any antibacterial effects and neither the resulting gC_3N_4-ZnO:Mn_1–0.1 solution.

Author contributions

Adriana Popa: conceptualization, validation, formal analysis, investigation, data curation, writing – original draft, writing – review& editing. Maria Stefan: conceptualization, formal analysis, investigation, writing – original draft, writing – review & editing. Sergiu Macavei: formal analysis, investigation. Lucian Barbu-Tudoran: formal analysis, investigation. Ioana Perhaita: formal analysis, investigation. Dana Toloman: conceptualization, validation, formal analysis, investigation, writing – original draft, writing – review & editing, supervision.

Conflicts of interest

The authors declare that they have no known competing financial interests or personal relationships that could have appeared to influence the work reported in this paper.

Data availability

All data have been provided in the main article and in supplementary information (SI) file.

The supplementary information contains: the influence of different concentrations of scavengers on the removal rate; XPS spectra; XRD diffractogram and FT-IR spectra of the sample before and after reusability tests. See DOI: https://doi.org/10.1039/d5ma01238d.

Acknowledgements

This work was supported through the ''Nucleu'' Program within the National Research Development and Innovation Plan 2022–2027, Romania, carried out with the support of MEC, project no. 27N/03.01.2023, component project code PN 23 24 01 03.

References

1 M. Kumar, V. P. Singh, S. B. Bhat and R. Kumar, Environmental risks of textile dyes and photocatalytic materials for sustainable treatment: current status and future directions, *Discov. Environ.*, 2025, **3**, 132, DOI: 10.1007/s44274-025-00337-0.
2 A. Garg and L. Chopra, Dye Waste: A significant environmental hazard, *Mater. Today Proc.*, 2022, **48**, 1310–1315, DOI: 10.1016/j.matpr.2021.09.003.
3 D. Liu, D. Chen, Z. Hao, Y. Tang, L. Jiang, T. Li, B. Tian, C. Yan, Y. Luo and B. Jia, Efficient degradation of Rhodamine B in water by $CoFe_2O_4/H_2O_2$ and $CoFe_2O_4$/PMS systems: A comparative study, *Chemosphere*, 2022, **307**, 135935, DOI: 10.1016/j.chemosphere.2022.135935.
4 S. Mishra and B. Sundaram, A review of the photocatalysis process used for wastewater treatment, *Mater. Today Proc.*, 2024, **102**, 393–409, DOI: 10.1016/j.matpr.2023.07.147.
5 S. A. Sergiienko, D. M. Tobaldi, L. Lajaunie, D. V. Lopes, G. Constantinescu, A. L. Shaula, N. D. Shcherban, V. I. Shkepu, J. J. Calvino, J. R. Frade, J. A. Labrincha and A. V. Kovalevsky, Photocatalytic removal of benzene over Ti_3C_2Tx MXene and TiO_2–MXene composite materials under solar

and NIR irradiation, *J. Mater. Chem. C*, 2022, **10**, 626–639, DOI: 10.1039/D1TC03826E.

6 G. Xia, Y. Lam, S. Fan, X. Bian, P. Qi, Z. Qiao, K. Ma and J. H. Xin, Recent advances in cotton fabric-based photocatalytic composites for the degradation of organic contaminants, *Carbohydr. Polym.*, 2024, **332**, 121872, DOI: 10.1016/j.carbpol.2024.121872.

7 O. Pana, A. Petran, A. Popa, M. Stefan, T. D. Silipas, C. Leostean, B. S. Vasile, F. Pogacean and D. Toloman, $Zn_xFe_{3-x}O_4$–ZnO heterojunction interfaced with poly(L-DOPA) electron transfer mediator layer for enhanced visible light photocatalytic activity, *J. Alloys Compd.*, 2024, **986**, 174168, DOI: 10.1016/j.jallcom.2024.174168.

8 C. B. Ong, L. Y. Ng and A. W. Mohammad, A review of ZnO nanoparticles as solar photocatalysts: Synthesis, mechanisms and applications, *Renewable Sustainable Energy Rev.*, 2018, **81**, 536–551, DOI: 10.1016/j.rser.2017.08.020.

9 Y. Sun, W. Zhang, Q. Li, H. Liu and X. Wang, Preparations and applications of zinc oxide based photocatalytic materials, *Adv. Sens. Energy Mater.*, 2023, **2**, 100069, DOI: 10.1016/j.asems.2023.100069.

10 Z. Mirzaeifard, Z. Shariatinia, M. Jourshabani and S. M. R. Darvishi, ZnO Photocatalyst Revisited: Effective Photocatalytic Degradation of Emerging Contaminants Using S-Doped ZnO Nanoparticles under Visible Light Radiation, *Ind. Eng. Chem. Res.*, 2020, **59**, 15894–15911, DOI: 10.1021/acs.iecr.0c03192.

11 S. Yuvaraj, A. C. Fernandez, M. Sundararajan, C. S. Dash and P. Sakthivel, Hydrothermal synthesis of ZnO–CdS nanocomposites: structural, optical and electrical behavior, *Ceram. Int.*, 2020, **46**(1), 391–402, DOI: 10.1016/j.ceramint.2019.08.274.

12 S. Pourali, R. Amrollahi, S. Alamolhoda and S. M. Masoudpanah, In situ synthesis of ZnO/g-C3N4 based composites for photodegradation of methylene blue under visible light, *Sci. Rep.*, 2025, **15**, 462, DOI: 10.1038/s41598-024-84645-0.

13 A. Tarighati Sareshkeh, M. S. Seyed Dorraji, Z. Karami, S. Shahmoradi, E. Fekri, H. Daneshvar, M. H. Rasoulifard and D. N. Karimov, Preparation of high-crystalline and non-metal modified g-C_3N_4 for improving ultrasound-accelerated white-LED-light-driven photocatalytic performances, *Sci. Rep.*, 2023, **13**, 15079, DOI: 10.1038/s41598-023-41473-y.

14 F. Hassan, S. N. Backer, I. W. Almanassra, M. A. Atieh, M. Elbahri and A. Shanableh, Solar-matched S-scheme ZnO/g-C3N4 for visible light-driven paracetamol degradation, *Sci. Rep.*, 2024, **14**, 12220, DOI: 10.1038/s41598-024-60306-0.

15 X. Gao, B. Yang, W. Yao, Y. Wang, R. Zong, J. Wang, X. Li, W. Jin and D. Tao, Enhanced photocatalytic activity of ZnO/g-C3N4 composites by regulating stacked thickness of g-C3N4 nanosheets, *Environ. Pollut.*, 2020, **257**, 113577, DOI: 10.1016/j.envpol.2019.113577.

16 K. Bi, X. Qin, S. Cheng and S. Liu, ZnO/g-C_3N_4 S scheme photocatalytic material with visible light response and enhanced photocatalytic performance, *Diamond Related Mater.*, 2023, **137**, 110143, DOI: 10.1016/j.diamond.2023.110143.

17 Z. Khoshsepehr, S. Alinejad and M. Alimohammadlou, Exploring industrial waste management challenges and smart solutions: An integrated hesitant fuzzy multi-criteria decision-making approach, *J. Cleaner Prod.*, 2023, **420**, 138327, DOI: 10.1016/j.jclepro.2023.138327.

18 L. Zhan, O. Li and Z. Xu, Preparing nano-zinc oxide with high-added-value from waste zinc manganese battery by vacuum evaporation and oxygen-control oxidation, *J. Cleaner Prod.*, 2020, **251**, 119691, DOI: 10.1016/j.jclepro.2019.119691.

19 H. Dave, N. Shaikh and P. Pamidimukkala, ZnO nanostructures grown from spent batteries: Ambient catalytic aspects and novel mechanistic insights, *Environ. Nanotechnol., Monit. Manage.*, 2024, **22**, 101004, DOI: 10.1016/j.enmm.2024.101004.

20 M. Stefan, B. Kocabas, A. Güngör, D. Toloman, A. M. Rostas, R. C. Suciu, S. Macavei, I. Ganea, I. Perhaita, S. Tripon, C. Leostean, E. Erdem and A. Popa, Manganese-doped Zinc Oxide recycled from spent alkaline batteries for photocatalysis and supercapacitor applications, *J. Energy Storage*, 2024, **99**, 113419, DOI: 10.1016/j.est.2024.113419.

21 S. C. Yan, Z. S. Li and Z. G. Zou, Photodegradation Performance of g-C_3N_4 Fabricated by Directly Heating Melamine, *Langmuir*, 2009, **25**(17), 10397–10401, DOI: 10.1021/la900923z.

22 A. Muthuganesh, I. Davis Jacob, J. P. Soundranayagam, S. Surender, P. Elangovan and X. H. Flora, Fabrication of g-C_3N_4/CuS heterostructures for efficient visible light-driven photocatalysts, *Inorg. Chem. Commun.*, 2024, **159**, 111813, DOI: 10.1016/j.inoche.2023.111813.

23 T. Alizadeh, S. Nayerib and N. Hamidia, Graphitic carbon nitride (g-C_3N_4)/graphite nanocomposite as an extraordinarily sensitive sensor for sub-micromolar detection of oxalic acid in biological samples, *RSC Adv.*, 2019, **9**, 13096, DOI: 10.1039/c9ra00982e.

24 K. I. John, T. B. Issa, A. N. Nikoloski, G. Ho and D. Li, Boosting visible-light photocatalytic activity of exfoliated g-C_3N_4 by a facile strategy coupling ion intercalation and thermal treatment, *Emergent Mater.*, 2025, **8**, 5777–5797, DOI: 10.1007/s42247-025-01178-6.

25 X. Guo, J. Duan, C. Li, Z. Zhang and W. Wang, Highly efficient Z-scheme gC_3N_4/ZnO photocatalysts constructed by co-melting-recrystallizing mixed precursors for wastewater treatment, *J. Mater. Sci.*, 2020, **55**, 2018–2031, DOI: 10.1007/s10853-019-04097-0.

26 K. Ravichandran, K. Shantha Seelan, P. Kavitha and S. Sriram, Influence of Cu + gC3N4 incorporation on the photocatalytic dye decomposition of ZnO film coated on stainless steel wire meshes, *J. Mater. Sci: Mater. Electron.*, 2019, **30**, 19703–19717, DOI: 10.1007/s10854-019-02321-w.

27 M. Sayed, B. Zhu, P. Kuang, X. Liu, B. Cheng, A. A. A. Ghamdi, S. Wageh, L. Zhang and J. Yu, EPR investigation on electron transfer of 2D/3D g-C_3N_4/ZnO S-scheme heterojunction for enhanced CO_2 photoreduction, *Adv. Sustainable Syst.*, 2022, **6**, 2100264, DOI: 10.1002/adsu.202100264.

28 P. Xia, B. Cheng, J. Jiang and H. Tang, Localized π-conjugated structure and EPR investigation of g-C3N4 photocatalyst, *Appl. Surf. Sci.*, 2019, **487**, 335–342, DOI: 10.1016/j.apsusc.2019.05.064.

29 E. A. Batista, A. C. Almeida Silva, T. K. de Lima, E. Vinicius Guimarães, R. Souza da Silva and N. Oliveira Dantas, Effect of the location of Mn^{2+} ions in the optical and magnetic properties of ZnO nanocrystals, *J. Alloys Compd.*, 2021, **850**, 156611, DOI: 10.1016/j.jallcom.2020.156611.

30 G. Mamba and A. K. Mishra, Graphitic carbon nitride ($g\text{-}C_3N_4$) nanocomposites: a new and exciting generation of visible light driven photocatalysts for environmental pollution remediation, *Appl. Catal., B*, 2016, **198**, 347–377, DOI: 10.1016/j.apcatb.2016.05.052.

31 M. J. Hakimi-Tehrani, S. A. Hassanzadeh-Tabrizi, N. Koupaei, A. Saffar-Teluri and M. Rafiei, Facile thermal synthesis of $g\text{–}C_3N_4$/ZnO nanocomposite with antibacterial properties for photodegradation of Methylene blue, *Mater. Res. Express*, 2021, **8**, 125002, DOI: 10.1088/2053-1591/ac3c71.

32 J. Jassi, S. Deepa, C. S. Chitra Lekha and N. Mariam Paul, Influence of $g\text{-}C_3N_4$ on the structural, optical, and morphological features of $g\text{-}C_3N_4$/ZnO nanocomposites, *Result. Surf. Inter.*, 2025, **20**, 100608, DOI: 10.1016/j.rsurfi.2025.100608.

33 J. Bauri and R. Bilash Choudhary, Inflated electronic and optical assessment of gC_3N_4/ZnO nanocomposite as a potential emissive layer material for OLED application, *J. Mol. Struct.*, 2025, **1322**, 140471, DOI: 10.1016/j.molstruc.2024.140471.

34 A. Bosnjakovic and S. Schlick, Spin Trapping by 5,5-Dimethylpyrroline-N-oxide in Fenton Media in the Presence of Nafion Perfluorinated Membranes: Limitations and Potential, *J. Phys. Chem. B*, 2006, **110**, 10720–10728, DOI: 10.1021/jp061042y.

35 X. Tian, Z. Cai, Y. Sun, M. Xu and B. Zhu, First-principles investigation of the two-dimensional van der Waals $g\text{-}C_3N_4$/g-ZnO heterojunction: Enhancing the photocatalytic hydrogen evolution activity, *Surf. Interfaces*, 2024, **52**, 104919, DOI: 10.1016/j.surfin.2024.104919.

36 N. Chidhambaram and K. Ravichandran, Fabrication of ZnO/g-C3N4 nanocomposites for enhanced visible light driven photocatalytic activity, *Mater. Res. Express*, 2017, **4**, 075037, DOI: 10.1088/2053-1591/aa7abd.

37 M. A. Qamar, S. Shahid, M. Javed, S. Iqbal, M. Sher, A. Bahadur, M. M. AL-Anazy, A. Laref and D. Li, Designing of highly active g-C3N4/Ni-ZnO photocatalyst nanocomposite for the disinfection and degradation of the organic dye under sunlight radiations, *Colloids Surf., A*, 2021, **614**, 126176, DOI: 10.1016/j.colsurfa.2021.126176.

38 F. Hassan, S. N. Backer, I. W. Almanassra, M. A. Atieh, M. Elbahri and A. Shanableh, Solar-matched S-scheme ZnO/g-C3N4 for visible light-driven paracetamol degradation, *Sci. Rep.*, 2024, **14**, 12220, DOI: 10.1038/s41598-024-60306-0.

39 X. Gao, B. Yang, W. Yao, Y. Wang, R. Zong, J. Wang, X. Li, W. Jin and D. Tao, Enhanced photocatalytic activity of ZnO/g-C3N4 composites by regulating stacked thickness of g-C3N4 nanosheets, *Environ. Pollut.*, 2020, **257**, 113577, DOI: 10.1016/j.envpol.2019.113577.

40 M. A. Qamar, S. Shahid, M. Javed, M. Sher, S. Iqbal, A. Bahadur and D. Li, Fabricated novel g-C3N4/Mn doped ZnO nanocomposite as highly active photocatalyst for the disinfection of pathogens and degradation of the organic pollutants from wastewater under sunlight radiations, *Colloids Surf., A*, 2021, **611**, 125863, DOI: 10.1016/j.colsurfa.2020.125863.